Nano Energy 77 (2020) 105157

Contents lists available at ScienceDirect

Nano Energy

journal homepage: http://www.elsevier.com/locate/nanoen

Hybridizing Li@Mn_6 and Sb@Ni_6 superstructure units to tune the electrochemical performance of Li-rich layered oxides

Yiwei Li [a,1], Lin Xie [b,1], Ze Zheng [a], Zu-Wei Yin [a], Jianyuan Li [a,d], Mouyi Weng [a], Jiajie Liu [a], Jiangtao Hu [a], Kai Yang [a], Guoyu Qian [a], Bo Cao [a], Zhibo Li [a], Shenyang Xu [a], Wenguang Zhao [a], Shunning Li [a], Junliang Sun [d], Mingjian Zhang [a,c,**], Feng Pan [a,*]

[a] School of Advanced Materials, Peking University, Shenzhen Graduate School, Shenzhen, 518055, People's Republic of China
[b] Department of Physics, Southern University of Science and Technology, Shenzhen, 518055, People's Republic of China
[c] Center for Advanced Radiation Source (ChemMatCARS), The University of Chicago, Argonne, Illinois, 60439, United States
[d] College of Chemistry and Molecular Engineering, Peking University, Beijing, 100871, China

ARTICLE INFO

Keywords:
Superstructure unit
Local oxygen environment
Composited Li-Rich layered cathode
Electronic structure calculation

ABSTRACT

Li@Mn_6 superstructure units from the model compound Li_2MnO_3, i.e., six MnO_6 octahedra linked like a ring (Mn_6) with a central LiO_6 octahedron, could provide extra capacity when composited with other transition metal octahedra (TMO_6) structure units in Li and Mn-rich TM layered oxides, $xLi_2MnO_3{\cdot}(1\text{-}x)LiTMO_2$, one of the most promising high-energy-density cathodes. Nevertheless, it suffers serious capacity and voltage fade due to the unstable local oxygen environment in the basic superstructure unit Li@Mn_6. Herein, a new Li-rich layered oxide cathode, $Li(Li_{1/6}Mn_{1/3}Ni_{1/3}Sb_{1/6})O_2$, was designed and synthesized by compositing Li@Mn_6 with a similar superstructure unit Sb@Ni_6. Complementary structural/chemical analysis combining with the electronic structure calculations reveal that, the uniform mixing of these two superstructure units at the atomic level has been firstly accomplished in TM layers, which introduces a large amount of boundaries between Li@Mn_6 and Sb@Ni_6 superunits, thus greatly enriching the local oxygen environments, and reducing the energy barrier of Li^+ diffusion. Therefore, the better electrochemical performance, especially the superb cycling stability with the larger capacity (double that of $Li(Ni_{2/3}Sb_{1/3})O_2$) is implemented. It provides another route to design new Li-rich layered oxides with the better cycling stability by modifying local oxygen environments.

1. Introduction

In recent years, energy storage has become more and more urgent facing to the global warming and the shortage of fossil fuel. Lithium ion batteries (LIBs), due to the high energy density and safety, are considered as one of candidates for the next-generation energy storage devices [1,2]. Nevertheless, the energy density, cycle life and safety of LIBs still could not meet the explosive-growing market requirements, especially for electric vehicles, stationary energy storages, and so on [3–5]. One crucial challenge is to search new cathodes with high energy density. Currently, transition metal (TM) layered oxides are widely considered owing to their high theoretical capacities [6–10]. Structure unit, which means the lattice atom and its coordination environment, determines the electrochemical performance of TM layered oxides to a great extent [11]. Therefore, to design new cathode materials from different structure units is an effective way to obtain the next-generation cathodes with high performance.

Li@Mn_6 superstructure unit from a model layered oxide Li_2MnO_3, in which six MnO_6 octahedra are linked like a ring (Mn_6) with the central LiO_6 octahedron, could provide extra capacity when composited with other transition metal octahedra (TMO_6) structure units in $LiTMO_2$ (TM = Ni, Co, Mn). The superstructure, originated from the ordering of Li/Mn in the TM layers, will cause Li–O–Li connection configuration, which contributes to the oxygen redox during charging-discharging process. The superstructure in single-layer Li_2MnO_3 will be stable, however, it will become unstable when it gathers in domain [12–14]. As such, Li and Mn-rich TM layered oxides, which could be written as $xLi_2MnO_3.(1\text{-}x)LiTMO_2$ (TM = Ni, Co, Mn), exhibit high practical capacity (>250 mA h

* Corresponding author.
** Corresponding author. School of Advanced Materials, Peking University, Shenzhen Graduate School, Shenzhen, 518055, People's Republic of China.
E-mail addresses: zhangmj@pkusz.edu.cn (M. Zhang), panfeng@pkusz.edu.cn (F. Pan).
[1] These authors contributed equally to this work.

https://doi.org/10.1016/j.nanoen.2020.105157
Received 2 May 2020; Received in revised form 28 June 2020; Accepted 29 June 2020
Available online 11 July 2020

g^{-1}) and have become one of the most promising cathodes [15–20]. Oxygen redox reaction to Li_2MnO_3 (LLMO) component is responsible for the superior electrochemical activity [21–24]. Actually, the oxygen redox activity comes from the unique superstructure unit Li@Mn_6 ring in LLMO as compared to $LiTMO_2$ component. Nevertheless, the oxygen redox is partially irreversible due to the unstable local oxygen environment on Li@Mn_6 unit in Li and Mn-rich cathodes, i.e., each oxygen anion is surrounding with four Li ions and two Mn cations. It would lead to the irreversible lattice oxygen loss, and the structure degradation from the active layered phase to the inactive spinel phase, which initiated into the particle surface, and creeped into the bulk. Eventually, the fast capacity and voltage decay are observed during long-term cycling, which severely impede the practical application [25–27]. In brief, the unstable oxygen environment in Li@Mn_6 units can provide high capacity but fast capacity/voltage decay. To solve this concern, multiple methods including surface modification/coating [28–30], the layered/spinel heterostructure [31,32], and elemental doping (Al, Ti, Mg, etc.) [33–35], were developed. In principle, all these methods involve the modification of the local oxygen environment partially, which demonstrates the significance and effectiveness of tuning the local oxygen environment in solving the concern above.

Similar with Li@Mn_6 unit, another superstructure unit Sb@Ni_6 ring, in which six NiO_6 octahedra are linked like a ring (Ni_6) with the central SbO_6 octahedron, was reported in a sodium TM layered oxide cathode $Na(Ni_{2/3}Sb_{1/3})O_2$ for sodium ion batteries. The stable local oxygen environments, i.e., each oxygen anion is surrounding with three Na^+ ions, two Ni cations and one Sb cation, could not only promote the air stability and thermal stability, but also increase the redox potential and simplify the phase transition process during cycling [36,37]. As a prototype compound composing of Sb@Ni_6 superstructure unit for LIBs [38,39], Li$(Ni_{2/3}Sb_{1/3})O_2$ (LNSO) inherits the stable local oxygen environment, i.e., each oxygen anion is surrounding with three Li^+ ions, two Ni cations and one Sb cation. However, it could only deliver low capacity (<100 mA h g^{-1}) and poor cycling stability [40].

Li@Mn_6 in layered $Li(Ni_{0.5}Mn_{0.5})O_2$ to show 'inorganic aromaticity', originates from the direct delocalized interactions by Mn-d_{z2} orbitals with the super-exchange interactions by Mn–O–Mn, which has similar electronic behaviour with benzene-p_z does [41]. And Sb@Ni_6 in layered $Na(Ni_{2/3}Sb_{1/3})O_2$ shares *d*-electrons with each other by a strong Ni–O–Ni 90° super-exchange interaction [36]. In normal Li-rich TM layered oxides $xLi_2MnO_3.(1\text{-}x)LiTMO_2$, Li_2MnO_3 can keep an ordered superstructure Li@Mn_6 ring but $LiTMO_2$ has disordered Ni, Mn and Co arrangements due to their internal energy difference around 3.57 meV/atom, which is smaller than the entropy term (13.7 meV/atom) at 1000 K [42]. Thus, it is possible to obtain a new cathode material by combining Li@Mn_6 and Sb@Ni_6 superstructure units together, and also come up with fundamental questions. For example, whether Li@Mn_6 and Sb@Ni_6 are in the same layer or separator layers, and if both superstructure units are in the same layer, how to arrange the boundary and how to affect electrochemical properties?

Herein, we design and synthesize a new Li-rich layered oxide $Li(Li_{1/6}Mn_{1/3}Ni_{1/3}Sb_{1/6})O_2$ (LLMNSO) by mixing Li@Mn_6 and Sb@Ni_6 superstructure units together at the molar ratio of 1:1, which could also be written as $0.5Li(Li_{1/3}Mn_{2/3})O_2{\cdot}0.5Li(Ni_{2/3}Sb_{1/3})O_2$. Interestingly, the uniform mixing of these two units at the atomic level has been firstly accomplished in the same TM layer. The local oxygen environment is modified and activated due to the formation of boundaries between Sb@Ni_6 and Li@Mn_6, which can reduce the energy barrier of Li^+ diffusion and provide extra capacity. Different to the previously-reported Li-rich layered oxides, LLMNSO exhibits the high initial capacity (double that of LNSO) with the high initial coulombic efficiency about 90%, and the superb cycling stability. These findings provide a guidance for designing new cathodes with higher energy density and better cycling stability in LIBs by regulating the local oxygen environment.

2. Results and discussions

2.1. Design of composited Li-rich layered oxide

Fig. 1 shows the design process of LLMNSO. As shown in Fig. 1a, LNSO exhibits a typical layered structure with O′3 phase (space group C2/m). Li layers and TM layers alternately stack along the c axis. One TM layer is composed of Ni^{2+} and Sb^{5+} ions in the ratio of 2: 1. They distribute over honeycomb pattern composed of the superstructure unit $Sb^{5+}@Ni^{2+}{}_6$ six-membered rings, wherein Ni^{2+} cations in the vertex and Sb^{5+} cations in the center of the six-membered ring (Fig. 1b). As shown in Fig. 1c–d, LLMO has the similar crystal structure with LNSO. TM layers are also tiled from the similar superstructure unit $Li^+@Mn^{4+}{}_6$ six-membered rings. The only difference between these two units is that, the positions of Ni^{2+} and Sb^{5+} are substituted by Mn^{4+} and Li^+ in the six-membered rings. Due to the similar layered structure, it is feasible to composite them with the ratio of 1:1 to construct LLMNSO, maintaining the same structure. Moreover, Ni^{2+} and Mn^{4+} are expected to occupy the same site in this structure in LLMNSO as well as Sb^{5+} and Li^+, due to the mixture of $Sb^{5+}@Ni^{2+}{}_6$ unit and $Li^+@Mn^{4+}{}_6$ unit, as shown in Fig. 1e.

2.2. Enhanced electrochemistry in composited Li-rich layered oxide

Synchrotron X-ray diffraction (SXRD) was utilized to analyze the crystal structure of as-prepared materials. As shown in Fig. 2a–b and S1, the similar layered structure is validated by the similar patterns with that of LNSO, LLMO and LLMNSO. Moreover, no peak splitting in the pattern of LLMNSO indicates the good solid solution reaction between LLMO and LNSO, and the wider peak profiles hint the smaller grain size (Table S1). In addition, the similar superstructure peaks of LLMNSO and LNSO can be observed (insets of Fig. 2a–b), implying that the Sb@Ni_6 and Li@Mn_6 units have been preserved in LLMNSO. To clarify it, the model of the disordered LLMNSO structure is built, and the simulated XRD pattern is shown in Fig. S2. No superstructure peak between 20 and 30°could be observed, which further proves the existence of Sb@Ni_6 and Li@Mn_6 superstructure units in LLMNSO. It is worth noting that, the pure phase of LLMNSO can be obtained only at very high calcination temperature (1100 °C). Rietveld refinement was performed on XRD patterns of LNSO and LLMNSO, and the parameters were deposited in Table S1. The lattice parameters *a*, *b*, *c* of LLMNSO are all smaller than those of LNSO, due to the larger atomic radius of Ni^{2+} (0.69 Å) than that of Mn^{4+} (0.53 Å). SEM images of LNSO and LLMNSO are shown in Figs. S3a–b, respectively. Irregular morphology is observed for LNSO with the particle size <200 nm, while LLMNSO has the similar morphology and the larger particle size close to 1 μm, which may be due to the higher annealing temperature (1100 °C). High resolution transmission electron microscope (HRTEM) images of LNSO and LLMNSO are shown in Figs. S3c–d. Both LNSO and LLMNSO have perfect layers along the *c* direction, and the smaller 001 interplanar distance of LLMNSO (0.51 nm) as compared to that of LNSO (0.52 nm) is consistent with the smaller lattice parameter *c* (Table S1). The element compositions of LNSO and LLMNSO are characterized by energy dispersive spectrum (EDS), as shown in Fig. S4. The atomic ratio of Ni and Sb is close to 2:1 in LNSO, and the atomic ratio of Mn, Ni and Sb is nearly 2:2:1 in LLMNSO, which are well consistent with our design.

The charge/discharge profiles of LNSO and LLMNSO in the 1st cycle are shown in Fig. 2c. As for LNSO, one obvious voltage plateau is observed at around 4.1 V during charging, and the corresponding discharge plateau appears at 3.8 V, which is consistent with the cyclic voltammetry (CV) curve (Fig. S5a). The discharge capacity of LNSO is 95 mA h g^{-1}, which is much less than the theoretical capacity (225 mA h g^{-1}). In comparison, LLMNSO exhibits a smaller charge/discharge polarization, and the discharge capacity reaches 165 mA h g^{-1}, nearly double that of LNSO. Different to LNSO, there is a short plateau above 4.5 V (marked by the dashed magenta rectangle), which presumably comes from a small amount of oxygen redox, but is different to the

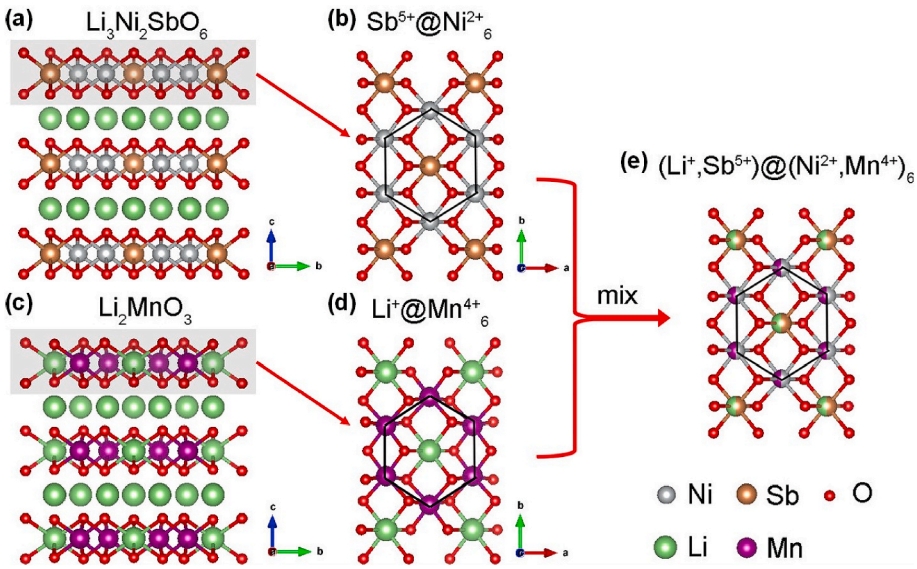

Fig. 1. Scheme illustration for designing new Li-rich layered oxide LLMNSO by compositing LNSO and LLMO. (a) The layered structure of LNSO perpendicular to *a* axis. (b) TM layer of LNSO showing the honeycomb pattern composed of the superstructure unit $Sb^{5+}@Ni^{2+}_6$. (c) The layered structure of LLMO perpendicular to *a* axis. (d) TM layer of LLMO showing the honeycomb pattern composed of the superstructure unit $Li^+@Mn^{4+}_6$. (e) The honeycomb pattern composed of (Li^+, Sb^{5+})@(Ni^{2+}, Mn^{4+})$_6$ unit in TM layer after mixing these two structure units together in LLMNSO.

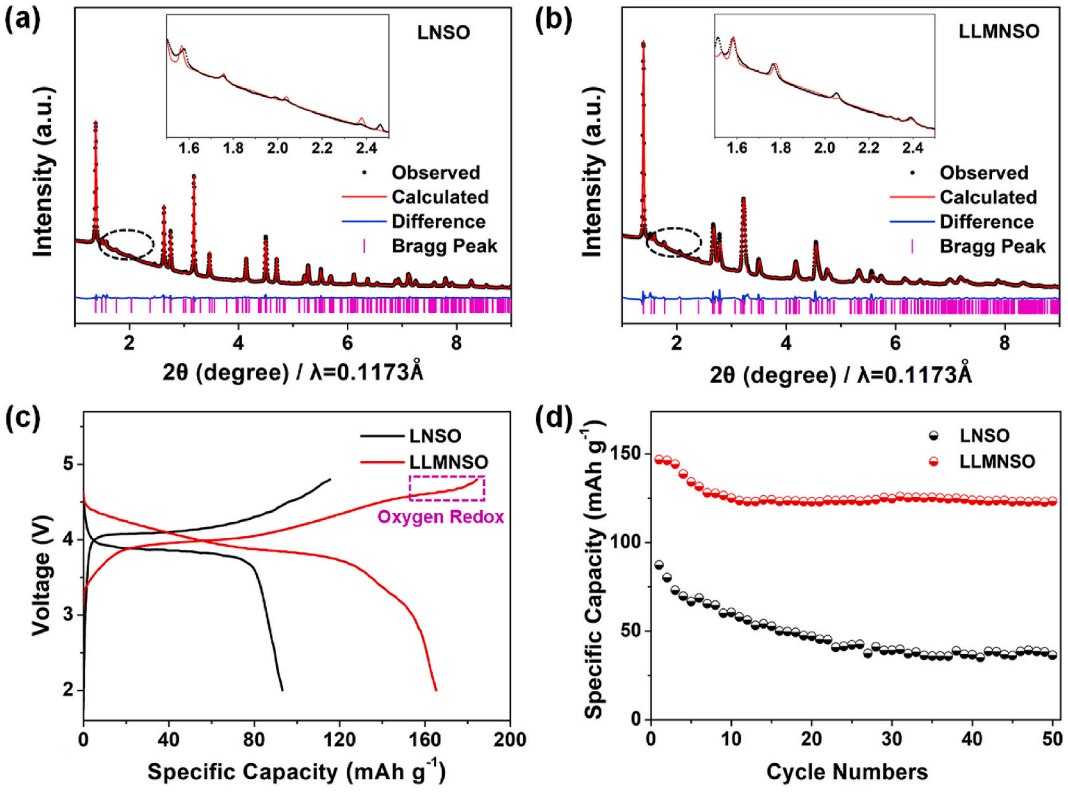

Fig. 2. The layered structures and the electrochemical performances of LNSO and LLMNSO. The synchrotron X-ray diffraction (SXRD) patterns and Rietveld refinements of LNSO (a) and LLMNSO (b). The superlattice peaks are marked by the black dashed circles, and magnified in the insets. (c) The charge/discharge profiles of LNSO and LLMNSO in the 1st cycle at 0.1 C (1 C = 200 mA g^{-1}) in the voltage range of 2.0–4.8 V. The region related to oxygen redox is marked by the magenta dashed rectangle. (d) The cycling stability of LNSO and LLMNSO at 0.1 C in the voltage range of 2.0–4.6 V.

previously-reported Li-rich layered oxides [43]. This phenomenon could also be validated in the CV curves of LLMNSO (Fig. S5b). An obvious wide oxidation peak appears above 4.5 V in LLMNSO at the first cycling, which corresponds to the short voltage plateau in Fig. 2c, implying the existence of oxygen redox [44,45]. Nevertheless, the intensity of this peak is much weaker when compared to the similar oxidation peak in CV curves of Li and Mn-rich cathodes reported recently [43], which also demonstrates that less oxygen redox in LLMNSO. The oxidation peak around 4.2 V and the reduction peak around 3.5 V in the first cycle correspond to Ni redox. The CV curves are similar during the following two cycles, one oxidation peak around 4.1 V and one reduction peak around 3.5 V could be observed, which corresponds to Ni^{2+}/Ni^{4+}. Therefore, the capacity of LLMNSO is originated from a large portion of TM redox and a small portion of oxygen redox. It can be further confirmed by X-ray photoelectron spectroscopy (XPS). Figs. S6–S7 display the X-ray photoelectron spectra of Ni 2*p* in LNSO and LLMNSO at different charge/discharge states during the 1st cycle. Ni $2p_{3/2}$ peak shifts to the high binding energy during charging and back to the low

binding energy during discharging for both cases. This demonstrates that the reversible redox of Ni cations during charging/discharging occurred in both LNSO and LLMNSO. To quantify the variation trend of Ni valence, Ni $2p_{3/2}$ peaks are divided into two sub-peaks (Ni^{2+} around 855 eV and Ni^{3+} around 856.5 eV) using mixed Gaussian−Lorentzian fitting. The relative content of Ni^{2+} in the samples is calculated by the peak area ratio of $Ni^{2+}/(Ni^{2+}+Ni^{3+})$ according to fitting results, and deposited in Tables S2–S3 for LNSO and LLMNSO. Stronger Ni redox reaction is observed in LLMNSO than LNSO, which is consistent with the larger capacity for LLMNSO.

The cycling performance of LNSO and LLMNSO at 0.1 C are compared in Fig. 2d. The capacity of LNSO fast decays from 87 to 36 mA h g^{-1} after 50 cycles, showing a low capacity retention of 41.3%. For LLMNSO, a small capacity degradation from 147 to 127 mA h g^{-1} occurs in the initial 8 cycles due to the initial surface reaction [46]. After that, about 97% of the capacity retention is observed in the following 42 cycles, displaying a superb cyclic stability. The HRTEM image of LLMNSO cathode after 10 cycles is shown in Fig. S8. It still maintains the well-aligned layered lattice in bulk, and only a little of spinel phase with the thickness of ~2 nm is observed at the particle surface, demonstrating its superb structure stability after long-term cycling. The cycling performance of LNSO and LLMNSO at 0.5 C in the voltage range of 2–4.6 V are shown in Fig. S9, LLMNSO also shows a much better rate performance compared to LNSO. The capacity retention could achieve to 87% after 100 cycles, demonstrating that LLMNSO could also exhibit superb cycling performance at high current density. The cycling stability should be greatly related to the structure evolution during cycling. To study the reason for the good cycling stability of LLMNSO, we tracked the structure variation in LNSO and LLMNSO during the 1st cycle through *ex situ* XRD. As shown in Fig. S10, XRD patterns of LNSO and LLMNSO under different charging/discharging states are presented. All the patterns are position-calibrated and intensity-normalized according to the strongest peak (around 65°) of Al current collector. To carefully examine the structure evolution, (001) peaks of LNSO and LLMNSO at different voltages are enlarged in Figs. S10c–d. It is obvious that the (001) peak of LNSO shifts a little after the 1st cycle, implying the irreversible structure evolution in LNSO. In comparison, (001) peak of LLMNSO returns to the original position after discharging, demonstrating a reversible structure

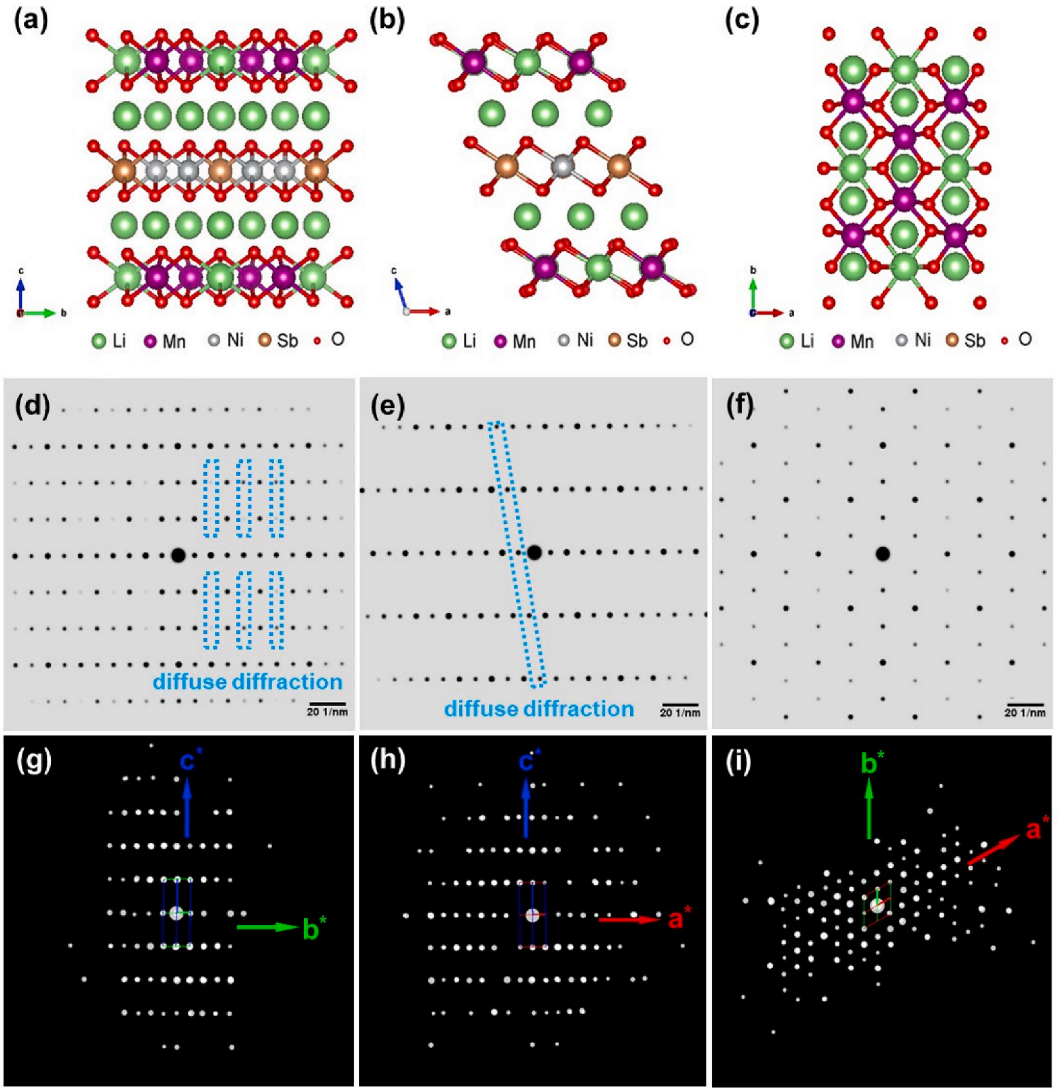

Fig. 3. Identification of the hybridization mode of Li@Ni_6 and Sb@Mn_6 by 3D electron diffraction. The illustration of the built model from *a* (a), *b* (b) and *c* (c) direction and the corresponding simulated electron diffraction images from *a* (d), *b* (e) and *c* (f) direction. The diffuse diffraction is marked by blue dashed rectangles. The built model is similar with the model shown in Fig. 1a, the differences are on the TM layers: One TM layer is composed of Sb@Ni_6 or Li@Mn_6 alone, and Li/Mn layer and Sb/Ni layer alternatively stack along the *c* direction. The simulated electron diffraction images were accomplished by CrystalMaker and SingleCrystal software from three lattice directions. The three-dimensional electron diffraction images from *a** (g), *b** (h) and *c** (i) direction of the same LLMNSO particle (shown at the lower right corner of Fig. S12). (For interpretation of the references to colour in this figure legend, the reader is referred to the Web version of this article.)

evolution for LLMNSO. To further quantify the variation, the peak position of the (001) peaks is plotted as a function of the voltage during charging (Fig. S11). For LNSO, it exhibits complex phase transition during charging, which may result in the poor cycling performance of LNSO. For LLMNSO, only two changes are observed with the increasing of the voltage, which is consistent with the previous reports about Li-rich cathodes [47,48]. Less structure transition may hint the stable structure for LLMNSO, thus the better cycling capability as compared to LNSO.

2.3. Atomic uniformity of structure units in TM layers

The different electrochemical behaviours between LLMNSO and the normal Li-rich cathodes might be attributed to the different local oxygen environments, which are determined by atomic arrangement in TM layers. In order to understand whether Li@Mn_6 and Sb@Ni_6 units are in the same TM layer or alternately stacking layer, the accurate crystal structure of LLMNSO is investigated by 3D electron diffraction technique, as shown in Fig. S12. To identify the structure, a possible structure model with the alternately stacking of Li@Mn_6 layer and Sb@Ni_6 layer (from LLMO and LNSO, respectively) along *c* direction is built in Fig. 3a–c, and the corresponding electron diffraction images along *a, b* and *c* direction are shown in Fig. 3d–f. As shown in Fig. 3d and e, the extra weak diffraction points called "diffuse diffraction" (marked by blue dashed rectangles) could be observed besides the strong diffraction points, which come from the stacking orderliness of TM layers along *c* direction [49]. The electron diffraction images of LLMNSO along the *a*, b** and *c** directions are clearly demonstrated in Fig. 3g–i. Compared with the model built, no diffuse diffraction points could be observed in diffraction images of LLMNSO from *a* and *b* direction (Fig. 3g and h), demonstrating the disordered atomic arrangement along the *c* direction. Thus, Li@Mn_6 and Sb@Ni_6 units are stacked in the same TM layer. In addition, owing to the dense diffraction points shown in Fig. 3i as compared with the sparse points simulated in Fig. 3f, the atomic arrangement in *ab* plane should be also disordered in LLMNSO.

In order to probe how Li@Mn_6 and Sb@Ni_6 units be arranged in the same layer, spherical aberration (Cs) corrected STEM was used to further explore the atomic arrangement of LLMNSO. As shown in Fig. 4a, the high-angle annual dark field (HAADF) and integrated differential phase contrast (iDPC) images of LLMNSO exhibits the perfect layered structure along the *c* direction. Owing to the great difference in atomic number of Li and Sb, their scattering cross sections will be extremely different, which will be reflected by contrast differences in HAADF and iDPC images. However, no apparent difference in contrast could be observed in TM layers, hinting that Li@Mn_6 unit and Sb@Ni_6 unit are uniformly mixed at the atomic level in the same TM layer. It is consistent with the results of 3D electron diffraction above. FFT map transformed from the iDPC image of LLMNSO (Fig. 4b) is shown in Fig. 4c. The weak diffraction spots in the dashed rectangles imply the existence of local ordered phase. The inverse FFT map from these weak diffraction points in Fig. 4c is presented in Fig. 4d. The ordered part could be observed (marked by the cyan circles), which might be due to the local segregation and enrichment of some Sb@Ni_6 units or Li@Mn_6 units. In brief, Sb@Ni_6 units and Li@Mn_6 units mainly distribute uniformly to a great extent in TM layer of LLMNSO.

2.4. Reversible oxygen redox revealed by XPS

The atomic uniformity of Sb@Ni_6 units and Li@Mn_6 units in TM layers has been confirmed by the local structure analysis above. Owing to such atomic mixing in TM layers of LLMNSO, the boundaries between Sb@Ni_6 and Li@Mn_6 units will be abundant, which would lead to a variety of local oxygen environments. O 1*s* XPS was utilized to distinguish these different oxygen environments in LNSO and LLMNSO electrodes. As shown in Fig. S13, we remove the Sb 3*d* peaks at the originated O 1*s* XPS spectra through peak fitting, to eliminate the overlapping of O signal and Sb signal. The treated XPS spectra of O 1*s* at different charge/discharge states during the 1st cycle are shown in Fig. 5 for LNSO and LLMNSO. As shown in Fig. 5a, only one distinct peak around 529.8 eV could be observed in the pristine electrode, which corresponds to the lattice oxygen in LNSO electrode [50]. During charging-discharging, no obvious change could be observed for this peak, demonstrating no oxygen redox involved. It is consistent with the pure Ni redox contribution to the electrochemistry above. Differently in Fig. 5b, two apparent peaks could be found in O 1*s* XPS spectra of LLMNSO, one peak around 529.7 eV (O1) and the other around 532.3 eV

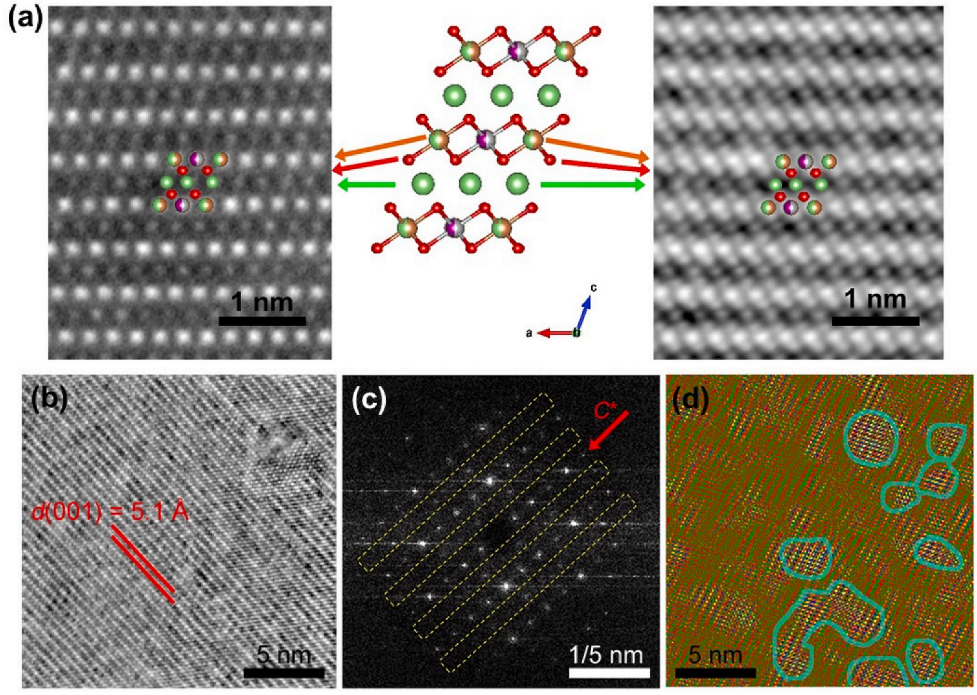

Fig. 4. Cs-corrected STEM analysis to reveal the structure details in the composited Li-rich layered oxides LLMNSO. (a) STEM HAADF image (left panel) and iDPC image (right panel) revealing the corresponding composited layered structure (middle panel) from the different aspects of atomic contrast. (b) iDPC image of LLMNSO. (c) FFT map transformed from the iDPC image in (b). The weak diffraction spots are observed in the dashed rectangles, hinting the existence of local ordered phase. (d) The inverse FFT map from the weak diffraction patterns in (c), indicating the local coexistence of ordered (highlighted by the cyan marks) and disordered phases. (For interpretation of the references to colour in this figure legend, the reader is referred to the Web version of this article.)

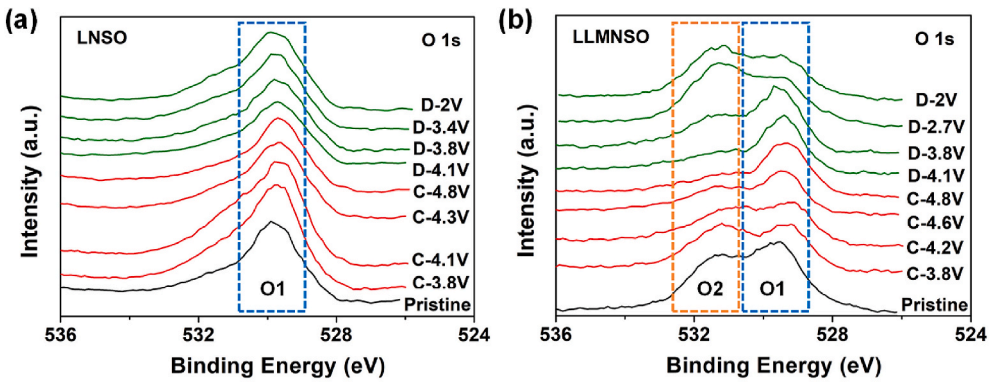

Fig. 5. Chemical analysis to reveal the reversible oxygen redox in LLMNSO. XPS spectra of O 1*s* in LNSO (a) and LLMNSO (b) electrodes at different charging-discharging voltages during the first cycling. O 1*s* peaks around 529.7 eV are defined as O1 (marked by blue dashed rectangle) and the peaks around 532.3 eV are defined as O2 (marked by orange dashed rectangle). (For interpretation of the references to colour in this figure legend, the reader is referred to the Web version of this article.)

(O2). Similarly, O1 peak comes from the lattice oxygen, and exhibits no obvious change during charging-discharging. Considering the diverse local oxygen environments in LLMNSO, O2 peak may arise from the oxygen anions at the boundaries between $Sb@Ni_6$ and $Li@Mn_6$ units, which exhibit different strengths of the cationic electrostatic bonds calculated by Pauling's rule when compared to oxygen anions in LNSO and LLMO [42]. During the 1st cycle, O2 peak intensity in LLMNSO decreases during charging and increases during discharging, implying the corresponding oxygen anions may possess electrochemical activity and contribute to the extra capacity of LLMNSO.

2.5. Modification of local oxygen environments

Based on the analysis above, more Li^+ ions could be involved in intercalation/deintercalation in LLMNSO as compared to LNSO, which is most likely due to the modification of local oxygen environment. To validate the hypothesis, the model structures with various oxygen environments are constructed, and the corresponding electronic structures are calculated based on DFT theory.

The local oxygen environments in LLMO, LNSO and LLMNSO are shown in Fig. 6. In LLMO with $Li@Mn_6$ unit (Fig. 6a), each oxygen anion

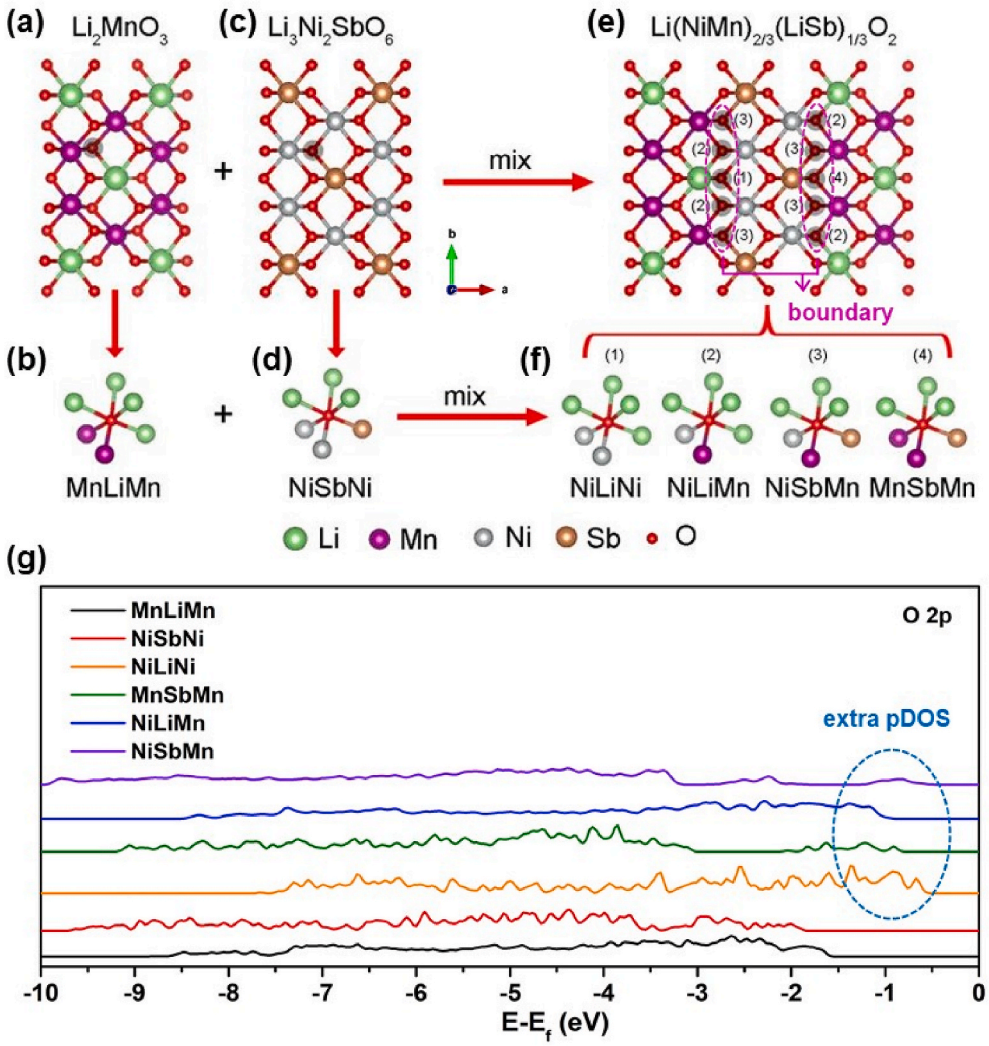

Fig. 6. Theoretical calculations to prove the modification of local oxygen environment in LLMNSO. (a) $Li@Mn_6$ unit in TM layer and (b) the corresponding local oxygen environment MnLiMn in LLMO. (c) $Sb@Ni_6$ unit in TM layer and (d) the corresponding local oxygen environment NiSbNi in LNSO. (e) The connected $Li@Mn_6$ and $Sb@Ni_6$ unit and their boundary (marked by pink dashed circle) in the TM layer of LLMNSO. (f) The emerging local oxygen environments originated from the boundary in (e), including NiLiNi, NiLiMn, NiSbMn, and MnSbMn. (g) Projected density of states (pDOS) of O 2*p* orbitals within the structure models containing the local oxygen environments of MiLiMn, NiSbNi, NiLiNi, MnSbMn, NiLiMn and NiSbMn, respectively. The extra pDOS from the oxygen anions in the local oxygen environments of NiLiNi, MnSbMn, NiLiMn and NiSbMn are marked by blue dashed circle. (For interpretation of the references to colour in this figure legend, the reader is referred to the Web version of this article.)

is connected by three Li ions in Li layer, and one Li ion and two Mn cations in TM layer (Fig. 6b), defined as MnLiMn. Similarly, in LNSO with Sb@Ni_6 unit (Fig. 6c), each oxygen anion is coordinated by three Li ions in Li layer, and one Sb cation and two Ni cations in TM layer (Fig. 6d), defined as NiSbNi. As shown in Fig. 6e, lots of boundaries between Li@Mn_6 and Sb@Ni_6 units (marked by the grey circles) appear in LLMNSO, which lead to the formation of four kinds of new local oxygen environments, as shown in Fig. 6f. These are defined as NiLiNi, NiLiMn, NiSbMn and MnSbMn, respectively. In brief, six kinds of local oxygen environments exist on LLMNSO, two of them are from Li@Mn_6 and Sb@Ni_6 unit, and the other four are from the boundary between in.

The DFT calculations are performed based on the models with the chosen six local oxygen environments (MnLiMn, NiSbNi, NiLiNi, MnSbMn, NiLiMn and NiSbMn), respectively, and the corresponding projected DOS (pDOS) of the oxygen 2*p* states are shown in Fig. 6g. Interestingly, extra pDOS contribution between −0.5 and −2.0 eV relative to the Fermi level (marked by the blue circle), could be observed for NiLiNi, MnSbMn, NiLiMn and NiSbMn, related to the boundary. We can deduce that, the oxygen anions at the boundary are more activating and easier to participate in electrochemical reaction. The similar phenomenon could also be observed in the pDOS of Ni 3*d* orbitals and Mn 3*d* orbitals, as shown in Fig. S14. Considering each Li^+ ion is connected by six oxygen ions in LLMNSO, lithium ions connected by oxygen anions at the boundary will be easier to diffuse. In other words, the modification of local oxygen environment at the boundary could reduce the energy barrier of Li^+ diffusion and provide more capacity during cycling. To further prove this conclusion, we also use NEB method to calculate the migration barrier of one Li-ion diffusion in different structure models of MiLiMn, NiSbNi, NiLiNi, MnSbMn, NiLiMn and NiSbMn, respectively. As shown in Table S4, the migration barrier of one Li-ion diffusion in NiLiNi, MnSbMn, NiLiMn and NiSbMn (related to the boundary) are lower than MnLiMn and NiSbNi, which also demonstrates that Li-ions connected by oxygen anions at the boundary will be easier to diffuse.

3. Conclusions

A new Li-rich layered oxide LLMNSO has been designed and successfully synthesized by composting two similar superstructure units Li@Mn_6 and Sb@Ni_6, which originated from LLMO and LNSO. It shows better electrochemical performance compared to LNSO, especially the doubled capacity and the excellent cycling stability. Combining the electron diffraction and Cs-STEM images, the atomic-level mixture of Li@Mn_6 and Sb@Ni_6 is implemented in the same TM layers of LLMNSO. Such a uniformity brings with a large number of boundaries between Li@Mn_6 and Sb@Ni_6 superstructure units, and introduces more local oxygen environments in LLMNSO. DFT calculations as well as the XPS results demonstrate that, these emerging local oxygen environments at the boundary exhibit more electrochemical activity, lower the energy barrier of Li diffusion and provide extra capacity. These findings provide new guidance for the development of new high-capacity positive electrode materials by modifying the local oxygen environments through multiple cations mixing.

Author contributions

Yiwei Li, with contributions from Jiajie Liu and Jiangtao Hu, designed and performed the research, supervised by Mingjian Zhang and Feng Pan. Ze Zheng, with help of Mouyi Weng and Shunning Li, did the DFT calculations. Jianyuan Li, Zuwei Yin and Junliang Sun, conducted 3D electron diffraction experiments. Lin Xie conducted spherical aberration (Cs) corrected scanning transmission electron microscope (STEM) experiments. Shenyang Xu and Wenguang Zhao conducted high resolution transmission electron microscope (HRTEM) experiments. Zhibo Li and Bo Cao, with contributions from Kai Yang and Guoyu Qian, conducted scanning electron microscope (SEM) and energy dispersive spectrometer (EDS) experiments. Yiwei Li, Mingjian Zhang and Feng Pan discussed the results and contributed to manuscript preparation.

Declaration of competing interest

The authors declare that they have no known competing financial interests or personal relationships that could have appeared to influence the work reported in this paper.

CRediT authorship contribution statement

Yiwei Li: Conceptualization, Writing - review & editing, Visualization, Supervision. **Lin Xie:** Data curation, Visualization, Supervision. **Ze Zheng:** Methodology, Visualization, Data curation. **Zu-Wei Yin:** Investigation, Data curation, Visualization. **Jianyuan Li:** Data curation, Visualization, Writing - original draft. **Mouyi Weng:** Methodology, Visualization. **Jiajie Liu:** Data curation, Visualization. **Jiangtao Hu:** Data curation, Supervision. **Kai Yang:** Visualization, Supervision. **Guoyu Qian:** Data curation, Visualization. **Bo Cao:** Data curation, Supervision. **Zhibo Li:** Visualization, Supervision. **Shenyang Xu:** Data curation, Visualization. **Wenguang Zhao:** Data curation, Visualization. **Shunning Li:** Methodology, Visualization, Supervision. **Junliang Sun:** Data curation, Visualization, Supervision. **Mingjian Zhang:** Data curation, Writing - review & editing, Visualization, Supervision. **Feng Pan:** Supervision, Writing - review & editing, Project administration, Funding acquisition.

Acknowledgments

This work was financially supported by National Key R&D Program of China (2016YFB0700600), Soft Science Research Project of Guangdong Province (No. 2017B030301013), Shenzhen Science and Technology Research Grant (ZDSYS201707281026184) and the Basic Research Program of Shenzhen (JCYJ20190809145205497) in China. This research used resources of the Advanced Photon Source, a U.S. Department of Energy (DOE) Office of Science User Facility operated for the DOE Office of Science by Argonne National Laboratory under Contract No. DE-AC02-06CH11357.

Appendix A. Supplementary data

Supplementary data to this article can be found online at https://doi.org/10.1016/j.nanoen.2020.105157.

References

[1] H. Wang, Y. Cui, Carbon Energy 1 (2019) 13–18.
[2] L. Chen, Y.F. Su, S. Chen, N. Li, L.Y. Bao, W.K. Li, Z. Wang, M. Wang, F. Wu, Adv. Mater. 26 (2014) 6756–6760.
[3] Y. Yuan, J. Lu, Carbon Energy 1 (2019) 8–12.
[4] C. Zhan, T.P. Wu, J. Lu, K. Amine, Energy Environ. Sci. 11 (2018) 243–257.
[5] F. Liu, C. Wang, X. Sui, M.A. Riaz, M. Xu, L. Wei, Y. Chen, Carbon Energy 1 (2019) 173–199.
[6] M. Li, J. Lu, Z.W. Chen, K. Amine, Adv. Mater. 30 (2018) 1800561.
[7] T. Or, S.W.D. Gourley, K. Kaliyappan, A. Yu, Z. Chen, Carbon Energy 2 (2020) 6–43.
[8] J.-I. Hata, M. Hirayama, K. Suzuki, N. Dupre, D. Guyomard, R. Kanno, Batter. Supercaps 2 (2019) 454–463.
[9] J. Kim, H. Cha, H. Lee, P. Oh, J. Cho, Batter. Supercaps 3 (2020) 309–322.
[10] S. Hy, H.D. Liu, M.H. Zhang, D.N. Qian, B.J. Hwang, Y.S. Meng, Energy Environ. Sci. 9 (2016) 1931–1954.
[11] J. Zheng, Y. Ye, F. Pan, Nat. Sci. Rev. 7 (2019) 242–245.
[12] Z.-L. Wu, H. Xie, Y. Li, F. Zhang, Z. Wang, W. Zheng, M. Yang, Z. Xu, Z. Lu, J. Alloys Compd. 827 (2020) 154202.
[13] J. Song, B. Li, Y. Chen, Y. Zuo, F. Ning, H. Shang, G. Feng, N. Liu, C. Shen, X. Ai, D. Xia, Adv. Mater. 32 (2020) 2000190.
[14] Y. Zuo, B. Li, N. Jiang, W. Chu, H. Zhang, R. Zou, D. Xia, Adv. Mater. 30 (2018) 1707255.
[15] C.S. Johnson, J.S. Kim, C. Lefief, N. Li, J.T. Vaughey, M.M. Thackeray, Electrochem. Commun. 6 (2004) 1085–1091.
[16] M.M. Thackeray, C.S. Johnson, J.T. Vaughey, N. Li, S.A. Hackney, J. Mater. Chem. 15 (2005) 2257–2267.

[17] Y. Zu-Wei, L. Jun-Tao, H. Ling, P. Feng, S. Shi-Gang, Chin. J. Struct. Chem. 39 (2020) 20–25.
[18] C.S. Johnson, N.C. Li, C. Lefief, J.T. Vaughey, M.M. Thackeray, Chem. Mater. 20 (2008) 6095–6106.
[19] F.Q. Cheng, Y.L. Xin, J.T. Chen, L. Lu, X.X. Zhang, H.H. Zhou, J. Mater. Chem. A 1 (2013) 5301–5308.
[20] N. Kireeva, V.S. Pervov, Batter. Supercaps 3 (2020) 427–438.
[21] A.R. Armstrong, M. Holzapfel, P. Novák, C.S. Johnson, S.H. Kang, M.M. Thackeray, P.G. Bruce, J. Am. Chem. Soc. 128 (2006) 8694–8698.
[22] S. Hy, F. Felix, J. Rick, W.N. Su, B.J. Hwang, J. Am. Chem. Soc. 136 (2014) 999–1007.
[23] H. Chen, M.S. Islam, Chem. Mater. 28 (2016) 6656–6663.
[24] S.H. Yu, T. Yoon, J. Mun, S. Park, Y.-S. Kang, J.-H. Park, S.M. Oh, Y.-E. Sung, J. Mater. Chem. A 1 (2013) 2833–2839.
[25] A. Boulineau, L. Simonin, J.F. Colin, E. Canevet, L. Daniel, S. Patoux, Chem. Mater. 24 (2012) 3558–3566.
[26] Z.H. Lu, J.R. Dahn, J. Electrochem. Soc. 149 (2002) A815–A822.
[27] M. Sathiya, A.M. Abakumov, D. Foix, G. Rousse, K. Ramesha, M. Saubanere, M. L. Doublet, H. Vezin, C.P. Laisa, A.S. Prakash, D. Gonbeau, G. VanTendeloo, J. M. Tarascon, Nat. Mater. 14 (2015) 230–238.
[28] M. Xu, Z. Chen, L. Li, H. Zhu, Q. Zhao, L. Xu, N. Peng, L. Gong, J. Power Sources 281 (2015) 444–454.
[29] F. Wu, J. Liu, L. Li, X. Zhang, R. Chen, ACS Appl. Mater. Interfaces 8 (2016) 23095–23104.
[30] B. Seteni, N. Rapulenyane, J.C. Ngila, S. Mpelane, H. Luo, J. Power Sources 353 (2017) 210–220.
[31] Y. Pei, C.-Y. Xu, Y.-C. Xiao, Q. Chen, B. Huang, B. Li, S. Li, L. Zhen, G. Cao, Adv. Funct. Mater. 27 (2017) 1604349.
[32] F.-D. Yu, L.-F. Que, Z.-B. Wang, Y. Zhang, Y. Xue, B.-S. Liu, D.-M. Gu, J. Mater. Chem. A 4 (2016) 18416–18425.
[33] P.K. Nayak, J. Grinblat, M. Levi, E. Levi, S. Kim, J.W. Choi, D. Aurbach, Adv. Energy Mater. 6 (2016) 1502398.
[34] R. Yu, X. Wang, Y. Fu, L. Wang, X. Yang, J. Mater. Chem. A 4 (2016) 4941–4951.
[35] X. Feng, Y. Gao, L. Ben, Z. Yang, Z. Wang, L. Chen, J. Power Sources 317 (2016) 74–80.
[36] P.F. Wang, M.Y. Weng, Y. Xiao, Z.X. Hu, Q.H. Li, M. Li, Y.D. Wang, X. Chen, X. N. Yang, Y.R. Wen, Y.X. Yin, X.Q. Yu, Y.G. Xiao, J.X. Zheng, L.J. Wan, F. Pan, Y. G. Guo, Adv. Mater. 31 (2019) 1903483.
[37] D. Yuan, X. Liang, L. Wu, Y. Cao, X. Ai, J. Feng, H. Yang, Adv. Mater. 45 (2014) 6301–6306.
[38] N. Twu, M. Metzger, M. Balasubramanian, C. Marino, L. Xin, H. Chen, H. Gasteiger, G. Ceder, Chem. Mater. 29 (2017) 2584–2593.
[39] N. Twu, X. Li, A. Urban, M. Balasubramanian, G. Ceder, Nano Lett. 15 (2014) 596–602.
[40] X.H. Ma, K.S. Kang, G. Ceder, Y.S. Meng, J. Power Sources 173 (2007) 550–555.
[41] Z.X. Hu, J.X. Zheng, C. Xin, G.F. Teng, Y.X. Zuo, F. Pan, J. Phys. Chem. C 122 (2018) 4125–4132.
[42] Z. Ze, W. Mou-Yi, Y. Lu-Yi, H. Zong-Xiang, C. Zhe-Feng, P. Feng, Chin. J. Struct. Chem. 38 (2019) 2020–2026.
[43] B. Strehle, K. Kleiner, R. Jung, F. Chesneau, M. Mendez, H.A. Gasteiger, M. Piana, J. Electrochem. Soc. 164 (2017) A400–A406.
[44] P.K. Nayak, J. Grinblat, M. Levi, B. Markovsky, Y. Wu, B. Powell, D. Aurbach, J. Electrochem. Soc. 161 (2014) A1534–A1547.
[45] R. Shunmugasundaram, R.S. Arumugam, J.R. Dahn, Chem. Mater. 27 (2015) 757–767.
[46] R.P. Qing, J.L. Shi, D.D. Xiao, X.D. Zhang, Y.X. Yin, Y.B. Zhai, L. Gu, Y.G. Guo, Adv. Energy Mater. 6 (2016) 1501914.
[47] S. Muhammad, H. Kim, Y. Kim, D. Kim, J.H. Song, J. Yoon, J.-H. Park, S.-J. Ahn, S.-H. Kang, M.M. Thackeray, Nano Energy 21 (2016) 172–184.
[48] D. Mohanty, S. Kalnaus, R.A. Meisner, K.J. Rhodes, J. Li, E.A. Payzant, D.L. Wood, C. Daniel, J. Power Sources 229 (2013) 239–248.
[49] D.A. Keen, A.L. Goodwin, Nature 521 (2015) 303–309.
[50] J.C. Dupin, D. Gonbeau, P. Vinatier, A. Levasseur, Phys. Chem. Chem. Phys. 2 (2000) 1319–1324.